

Strong chirality in twisted bilayer α-MoO_3

Bi-Yuan Wu(吴必园), Zhang-Xing Shi(石章兴), Feng Wu(吴丰), Ming-Jun Wang(王明军), and Xiao-Hu Wu(吴小虎)

Citation: Chin. Phys. B, 2022, 31 (**4**): 044101. DOI: 10.1088/1674-1056/ac3740
Journal homepage: http://cpb.iphy.ac.cn; http://iopscience.iop.org/cpb

What follows is a list of articles you may be interested in

High-sensitivity Bloch surface wave sensor with Fano resonance in grating-coupled multilayer structures

Daohan Ge(葛道晗), Yujie Zhou(周宇杰), Mengcheng Lv(吕梦成), Jiakang Shi(石家康), Abubakar A. Babangida, Liqiang Zhang(张立强), and Shining Zhu(祝世宁)

Chin. Phys. B, 2022, 31 (**4**): 044102. DOI: 10.1088/1674-1056/ac2e60

Determine the physical mechanism and source region of beat wave modulation by changing the frequency of high-frequency waves

Zhe Guo(郭哲), Hanxian Fang(方涵先), and Farideh Honary

Chin. Phys. B, 2022, 31 (**2**): 024103. DOI: 10.1088/1674-1056/ac422f

Estimation of co-channel interference between cities caused by ducting and turbulence

Kai Yang(杨凯), Zhensen Wu(吴振森), Xing Guo(郭兴), Jiaji Wu(吴家骥), Yunhua Cao(曹运华), Tan Qu(屈檀), and Jiyu Xue(薛积禹)

Chin. Phys. B, 2022, 31 (**2**): 024102. DOI: 10.1088/1674-1056/ac339c

High-confinement ultra-wideband bandpass filter using compact folded slotline spoof surface plasmon polaritons

Xue-Wei Zhang(张雪伟), Shao-Bin Liu(刘少斌), Ling-Ling Wang(王玲玲), Qi-Ming Yu (余奇明), Jian-Lou(娄健), and Shi-Ning Sun(孙世宁)

Chin. Phys. B, 2022, 31 (**1**): 014102. DOI: 10.1088/1674-1056/ac22a2

Tunable terahertz transmission behaviors and coupling mechanism in hybrid MoS_2 metamaterials

Yuwang Deng(邓雨旺), Qingli Zhou(周庆莉), Wanlin Liang(梁菀琳), Pujing Zhang(张朴婧), and Cunlin Zhang(张存林)

Chin. Phys. B, 2022, 31 (**1**): 014101. DOI: 10.1088/1674-1056/ac1fde

---

Strong chirality in twisted bilayer α-MoO_3

Bi-Yuan Wu(吴必园)[1,2], Zhang-Xing Shi(石章兴)[2], Feng Wu(吴丰)[3], Ming-Jun Wang(王明军)[1,4,†], and Xiao-Hu Wu(吴小虎)[2,‡]

[1] *School of Automation and Information Engineering, Xi'an University of Technology, Xi'an* 710048, *China*
[2] *Shandong Institute of Advanced Technology, Jinan* 250100, *China*
[3] *School of Optoelectronic Engineering, Guangdong Polytechnic Normal University, Guangzhou* 510665, *China*
[4] *School of Physics and Telecommunications Engineering, Shaanxi University of Technology, Hanzhong* 723001, *China*

(Received 26 September 2021; revised manuscript received 22 October 2021; accepted manuscript online 6 November 2021)

Chiral structures are promising in many applications, such as biological sensing and analytical chemistry, and have been extensively explored. In this paper, we theoretically investigate the chiral response of twisted bilayer α-MoO_3. Firstly, the analytical formula for the transmissivity is derived when the structure is illuminated with circularly polarized plane waves. Furthermore, the results demonstrate that the twisted bilayer α-MoO_3 can excite the strong chirality with the maximum circular dichroism (CD) of 0.89. In this case, the chirality is due to the simultaneous breaking the rotational symmetry and mirror symmetry, which originates from the relative rotation of two α-MoO_3 layers. To better understand the physical mechanism, the polarization conversion between the left-hand circular polarization (LCP) and right-hand circular polarization (RCP) waves is discussed as well. Moreover, it is found that the structure can maintain the strong chirality (CD $>$ 0.8) when the twisted angle varies from 69° to 80°, which effectively reduces the strictness in the requirement for rotation angle. In addition, the CD can be larger than 0.85 when the incidence angle of circularly polarized plane wave is less than 40°, implying that the chirality is robust against the angle of incidence. Our work not only provides an insight into chirality induced by the twisted bilayer α-MoO_3, but also looks forward to applications in biological sensing.

Keywords: chirality, twisted bilayer, α-MoO_3

PACS: 41.20.Jb, 11.30.Rd **DOI:** 10.1088/1674-1056/ac3740

1. Introduction

Chirality means that an object cannot coincide with its mirror image through any rotation or translation operation, which is widespread in nature.[1–3] Like human hands, the left hand does not overlap with the right hand that mirrors each other. The chiral enantiomers in drugs have the same chemical formula and physical properties, but they have different spatial arrangement. However, this asymmetry can lead to inactivity or even toxicity.[4] For example, the thalidomide incident in history results from insufficient understanding of chirality.[5] Therefore, it is very desirable to strengthen the ability to recognize the chiral objects.

The conventional technical means for distinguishing chiral structures is to measure the absorptivity/transmissivity spectra of their interactions with circularly polarized wave.[6] The difference in absorptivity/transmissivity between the left-hand circular polarization (LCP) and the right-hand circular polarization (RCP) is defined as circular dichroism (CD). Once the circular dichroism is detected, the chirality can be well judged. However, naturally occurring chirality is very weak, which would not only lead to the low sensitivity of measurement technology, but also result in the waste of materials and long acquisition time. Realizing the strong chirality is of critical importance in applications such as analytical chemistry,[7] polarization optics,[8–11] and biological sensing.[12–15] To obtain the strong chirality, many effective methods have been proposed.[16–21] Wang *et al.* designed a chiral structure combining bilayer of anisotropic metamaterial structures. Moreover, in that work it was proposed and proved that the destroying of the rotational and mirror symmetry simultaneously is the necessary condition for chiral structures through the framework of Jones calculus.[22] Their work provides a convincing theoretical basis for designing chiral structures. Based on Ref. [22], various bilayered chiral nanostructures have attracted great attention and been designed.[23–33] For example, Dong *et al*. proposed a chiral metamaterial composed of square-periodic array pairs of mutually twisted metallic crosses separated by dielectric layer.[34] Although the giant circular dichroism can be excited in chiral metamaterials, the fabrication of three-dimensional (3D) metamaterials is not easy.

In fact, the chiral response can be excited in the nanostructures with in-plane anisotropy. If there is a material with in-plane anisotropy itself, it will greatly simplify the chiral structures. The α-MoO_3 is a kind of naturally biaxial hyperbolic crystal with intrinsic in-plane anisotropy.[35–39] Furthermore, the fabrication of α-MoO_3 films is easier than that of 3D metamaterials. Chemical vapor transport technique with

†Corresponding author. E-mail: wangmingjun@xaut.edu.cn
‡Corresponding author. E-mail: xiaohu.wu@iat.cn

© 2022 Chinese Physical Society and IOP Publishing Ltd

low cost is often used to fabricate it. The α-MoO_3 has attracted a great deal of attention in recent decades for its profound applications in various disciplines, such as radiation heat transfers[40–42] and plasmonic biosensors.[43] Recently, Wu *et al*. studied extrinsic chirality resulting from the relative orientation of the α-MoO_3 film and the incident light in a single α-MoO_3 film,[39] where the CD (about 0.77) is still not strong enough. Combining with the viewpoint of the literature,[22] an idea about chirality based on the twisted bilayer structure comes into our mind. Very recently, Lin *et al*. realized chiral plasmons in van der Waals heterostructures comprised of twisted atomic bilayers,[44] which is determined by the interlayer quantum coupling. Stauber *et al*. investigated the chiral response in twisted bilayer graphene,[45] and the chiral character is associated with a longitudinal magnetic moment. Besides, the CD in Ref. [45] is extremely small (smaller than 0.001).

In this paper, we systematically investigate the chiral response of the twisted bilayer α-MoO_3. The thickness values of two α-MoO_3 slabs and the relative rotation angle between them are the two main parameters affecting the CD. In order to enhance the chirality of the structure, we optimize these parameters according to two methods. It is found that the CD of the structure can reach 0.89. Furthermore, the polarization conversion is calculated to reveal the underlying physical mechanism, which is completely different from the counterparts in Refs. [44,45]. Finally, the influence of the relative rotation angle and the angle of incidence on CD are studied as well.

2. Modeling and methods

Figure 1(a) schematically shows the model to be studied in this paper. The structure consists of two layers of α-MoO_3 with a relative rotation angle to break the overall mirror symmetry. In the figure, d_1 and d_2 are the thickness of the top and bottom α-MoO_3, respectively, and δ represents the relative rotation angle between the two α-MoO_3 slabs. The light incident is along the z direction. For the bottom α-MoO_3 slab, crystallographic axes [100], [001], and [010] are along the x, y, and z directions, respectively. Thus, the permittivity tensor can be expressed as $\varepsilon = \mathrm{diag}(\varepsilon_x, \varepsilon_y, \varepsilon_z)$. The expressions of ε_x, ε_y, and ε_z are described by the Lorentz equation[46] as follows:

$$\varepsilon_m = \varepsilon_{\infty,m}\left(1 + \frac{\omega_{\mathrm{LO},m}^2 - \omega_{\mathrm{TO},m}^2}{\omega_{\mathrm{TO},m}^2 - \omega^2 - \mathrm{j}\omega\Gamma_m}\right), \quad m = x, y, z, \tag{1}$$

where ω is angular frequency. The other parameters are[47] $\varepsilon_{\infty,x} = 4$, $\varepsilon_{\infty,y} = 5.2$, $\varepsilon_{\infty,z} = 2.4$, $\omega_{\mathrm{LO},x} = 1.8322 \times 10^{14}$ rad/s, $\omega_{\mathrm{LO},y} = 1.6041 \times 10^{14}$ rad/s, $\omega_{\mathrm{LO},z} = 1.8925 \times 10^{14}$ rad/s, $\omega_{\mathrm{TO},x} = 1.5457 \times 10^{14}$ rad/s, $\omega_{\mathrm{TO},y} = 1.0273 \times 10^{14}$ rad/s, $\omega_{\mathrm{TO},z} = 1.8058 \times 10^{14}$ rad/s, $\Gamma_x = \Gamma_y = 7.5398 \times 10^{11}$ rad/s, and $\Gamma_z = 3.7699 \times 10^{11}$ rad/s. Figure 1(b) depicts the real parts of the principal permittivities. One can see that the permittivities are greatly different from those in three principal directions, leading to the anisotropy in a wavelength range from 8 μm to 25 μm. For the top α-MoO_3 slab, there is a rotation angle δ relative to the bottom slab. Now, the permittivity tensor of the top slab can be described as

$$\varepsilon = \begin{bmatrix} \varepsilon_x \cos^2\delta + \varepsilon_y \sin^2\delta & (\varepsilon_x - \varepsilon_y)\sin\delta\cos\delta & 0 \\ (\varepsilon_y - \varepsilon_x)\sin\delta\cos\delta & \varepsilon_x \sin^2\delta + \varepsilon_y \cos^2\delta & 0 \\ 0 & 0 & \varepsilon_z \end{bmatrix}. \tag{2}$$

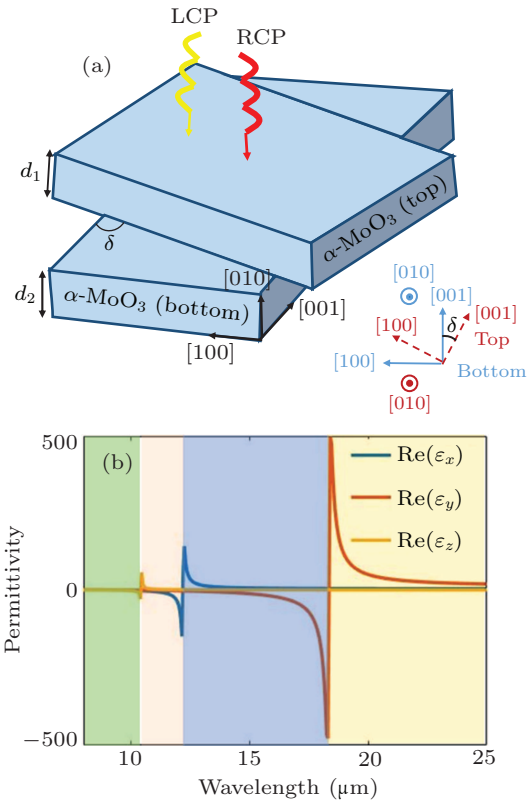


Fig. 1. (a) Schematic diagram of twisted bilayer α-MoO_3, (b) real parts of the principal permittivities of α-MoO_3.

The transfer matrix method (TMM) is used to calculate the transmissivity of the proposed structure.[47] According to Jones vector, elliptically polarization wave is defined as follows:

$$J(\psi, \eta) = \begin{pmatrix} \cos\psi \\ \mathrm{e}^{\mathrm{j}\eta}\sin\psi \end{pmatrix}, \tag{3}$$

where ψ is the angle between the incident plane and the electric field vector, and η is the phase difference between the electric fields parallel and perpendicular to the plane of incidence. The incident electric field is defined as

$$\boldsymbol{E}_{\mathrm{inc}} = \boldsymbol{u}\exp[-\mathrm{j}k_0 n_1(\sin\theta\cos\phi x + \sin\theta\sin\phi y + \cos\theta z)], \tag{4}$$

where

$$\begin{aligned} \boldsymbol{u} = {} & (\cos\psi\cos\theta\cos\varphi - \sin\psi\sin\theta\exp(\mathrm{j}\eta))\hat{x} \\ & + (\cos\psi\cos\theta\sin\varphi + \sin\psi\cos\theta\exp(\mathrm{j}\eta))\hat{y} \\ & - \cos\psi\sin\theta\hat{z}, \end{aligned} \tag{5}$$

where n_1 and n_2 represent the refractive index of incident medium and α-MoO_3 slab, respectively, ϕ is the azimuthal angle, and θ refers to the wave incidence angle.

The electric field in the incident medium ($z<0$) and that of transmitted wave ($z>d=d_1+d_2$) are calculated from

$$\begin{aligned}\boldsymbol{E}_1 &= \boldsymbol{E}_{\rm inc}+\boldsymbol{R}\exp[-{\rm j}(k_x x+k_y y-k_{1,z}z)],\\ \boldsymbol{E}_2 &= \boldsymbol{T}\exp[-{\rm j}(k_x x+k_y y+k_{2,z}(z-d))],\end{aligned} \tag{6}$$

where the electric field $\boldsymbol{E}_1$ consists of the incident electric field $\boldsymbol{E}_{\rm inc}$ and the reflected electric field with amplitude $\boldsymbol{R}$, and $\boldsymbol{T}$ is the electric field amplitude of the transmitted wave. Next, we discuss the wavevector components along the x, y, and z directions which can be written as

$$k_x = k_0 n_1 \sin\theta\cos\phi, \tag{7}$$

$$k_y = k_0 n_1 \sin\theta\sin\phi, \tag{8}$$

$$k_{1,z} = [(k_0 n_1)^2 - k_x^2 - k_y^2]^{1/2}, \tag{9}$$

$$k_{2,z} = [(k_0 n_2)^2 - k_x^2 - k_y^2]^{1/2}, \tag{10}$$

where k_0 is the wavevector in vacuum, $k_{1,z}$ and $k_{2,z}$ are the wavevector component along the z direction in $z<0$ and $z>d$, respectively. The electromagnetic fields in any α-MoO_3 slab are given by

$$E = [S_x(z)\hat{x}+S_y(z)\hat{y}+S_z(z)\hat{z}]\exp[-(k_x x+k_y y)], \tag{11}$$

$$\begin{aligned}H =& -{\rm j}\left(\frac{\varepsilon_0}{\mu_0}\right)^{1/2}[U_x(z)\hat{x}+U_y(z)\hat{y}+U_z(z)\hat{z}]\\ &\times\exp[-{\rm j}(k_x x+k_y y)],\end{aligned} \tag{12}$$

where S_x, S_y, S_z, U_x, U_y, and U_z are the amplitudes of electromagnetic field components. ε_0 and μ_0 represent the permittivity and permeability of vacuum, respectively. Supposing that the permittivity tensor of one anisotropic slab is

$$\boldsymbol{\varepsilon} = \begin{bmatrix}\varepsilon_{xx} & \varepsilon_{xy} & 0\\ \varepsilon_{yx} & \varepsilon_{yy} & 0\\ 0 & 0 & \varepsilon_{zz}\end{bmatrix}, \tag{13}$$

and substituting Eqs. (11) and (12) into the Maxwell's equations, we can obtain the following differential equation:

$$\frac{\rm d}{{\rm d}z}\begin{pmatrix}U_x\\ S_x\\ S_y\\ U_y\end{pmatrix} = k_0\boldsymbol{A}\begin{pmatrix}U_x\\ S_x\\ S_y\\ U_y\end{pmatrix}, \tag{14}$$

$$\boldsymbol{A} = \begin{bmatrix}0 & -K_xK_y-\varepsilon_{yx} & K_x^2-\varepsilon_{yy} & 0\\ -K_xK_y/\varepsilon_{zz} & 0 & 0 & K_xK_x/\varepsilon_{zz}-1\\ 1-K_yK_y/\varepsilon_{zz} & 0 & 0 & K_yK_x/\varepsilon_{zz}\\ 0 & \varepsilon_{xx}-K_y^2 & \varepsilon_{xy}K_yK_x & 0\end{bmatrix}, \tag{15}$$

where $K_x=k_x/k_0$ and $K_y=k_y/k_0$. For the bottom layer, the ε_{xy} and ε_{yx} are both equal to zero. For the top layer, ε_{xy} and ε_{yx} are non-zero complex numbers related to the rotation angle δ, which can be found in Eq. (2). By calculating the matrix $\boldsymbol{A}$, we can obtain the eigenvalues q_m and the eigenvector matrix $\boldsymbol{W}$. The tangential electromagnetic field components are described as

$$\begin{aligned}U_x(z) =& \sum_{m=1}^{2} w_{1,m}c_m^+\exp(k_0 q_m z)\\ &+\sum_{m=1}^{2} w_{1,m+2}c_m^-\exp[k_0 q_{m+2}(z-d)],\end{aligned} \tag{16}$$

$$\begin{aligned}U_y(z) =& \sum_{m=1}^{2} w_{2,m}c_m^+\exp(k_0 q_m z)\\ &+\sum_{m=1}^{2} w_{2,m+2}c_m^-\exp[k_0 q_{m+2}(z-d)],\end{aligned} \tag{17}$$

$$\begin{aligned}S_x(z) =& \sum_{m=1}^{2} w_{3,m}c_m^+\exp(k_0 q_m z)\\ &+\sum_{m=1}^{2} w_{3,m+2}c_m^-\exp[k_0 q_{m+2}(z-d)],\end{aligned} \tag{18}$$

$$\begin{aligned}S_y(z) =& \sum_{m=1}^{2} w_{4,m}c_m^+\exp(k_0 q_m z)\\ &+\sum_{m=1}^{2} w_{4,m+2}c_m^-\exp[k_0 q_{m+2}(z-d)],\end{aligned} \tag{19}$$

where $w_{i,m}$ $(i=1,2,3,4)$ are the elements of matrix $\boldsymbol{W}$. For the eigenvalues q_m, there are ${\rm Re}(q_1)<0$, ${\rm Re}(q_2)<0$, ${\rm Re}(q_3)>0$, and ${\rm Re}(q_4)>0$. For the bilayer slabs, all the boundary conditions as follows:

$$\begin{aligned}&\begin{pmatrix}\sin\psi\exp({\rm j}\eta)\\ {\rm j}\sin\psi n_1\cos\theta\exp({\rm j}\eta)\\ \cos\psi\cos\theta\\ -{\rm j}\cos\psi n_1\end{pmatrix}+\begin{bmatrix}1 & 0\\ -{\rm j}Y_1 & 0\\ 0 & -{\rm j}Z_1\\ 0 & 1\end{bmatrix}\begin{pmatrix}r_{\rm s}\\ r_{\rm p}\end{pmatrix}\\ &= \boldsymbol{B}\boldsymbol{W}_1\begin{bmatrix}\boldsymbol{I} & \boldsymbol{0}\\ \boldsymbol{0} & \boldsymbol{X}_1\end{bmatrix}\begin{pmatrix}c_1^+\\ c_1^-\end{pmatrix},\end{aligned} \tag{20}$$

where

$$\boldsymbol{B} = \begin{pmatrix}0 & -F_{\rm s} & F_{\rm c} & 0\\ -F_{\rm c} & 0 & 0 & -F_{\rm s}\\ 0 & F_{\rm c} & F_{\rm s} & 0\\ F_{\rm s} & 0 & 0 & -F_{\rm c}\end{pmatrix}, \tag{21}$$

$$\boldsymbol{B}\boldsymbol{W}_1\begin{bmatrix}\boldsymbol{V}_1 & \boldsymbol{0}\\ \boldsymbol{0} & \boldsymbol{I}\end{bmatrix}\begin{pmatrix}c_1^+\\ c_1^-\end{pmatrix} = \boldsymbol{B}\boldsymbol{W}_2\begin{bmatrix}\boldsymbol{V}_1 & \boldsymbol{0}\\ \boldsymbol{0} & \boldsymbol{X}_2\end{bmatrix}\begin{pmatrix}c_2^+\\ c_2^-\end{pmatrix}, \tag{22}$$

$$\boldsymbol{B}\boldsymbol{W}_2\begin{bmatrix}\boldsymbol{V}_2 & \boldsymbol{0}\\ \boldsymbol{0} & \boldsymbol{I}\end{bmatrix}\begin{pmatrix}c_2^+\\ c_2^-\end{pmatrix} = \begin{pmatrix}\boldsymbol{I} & 0\\ {\rm j}Y_2 & 0\\ 1 & {\rm j}Z_2\\ 0 & \boldsymbol{I}\end{pmatrix}\begin{pmatrix}t_{\rm s}\\ t_{\rm p}\end{pmatrix}. \tag{23}$$

In Eqs. (22) and (23), $\boldsymbol{W}_1$ and $\boldsymbol{W}_2$ are the eigenvectors of the matrix $\boldsymbol{A}$ for the top layer and the bottom layer, respectively; $\boldsymbol{I}$ and $\boldsymbol{0}$ are identity matrix and zero matrix, respectively; c_1^+, c_2^+, c_1^-, and c_2^- are unknown constants, $\boldsymbol{X}_1$, $\boldsymbol{X}_2$, $\boldsymbol{V}_1$, and $\boldsymbol{V}_2$ are diagonal matrices with diagonal elements $\exp(-k_0 q_{2+m}^1 d_1)$, $\exp(-k_0 q_{2+m}^2 d_2)$, $\exp(k_0 q_m^1 d_1)$, and $\exp(k_0 q_m^2 d_2)$, $m = 1, 2$, with q_{2+m}^1 and q_m^1 being the eigenvalues of matrix $\boldsymbol{A}$ for the top layer, while q_{2+m}^2 and q_m^2 denoting the eigenvalues of matrix $\boldsymbol{A}$ for the bottom layer; $F_s = k_y/\sqrt{k_x^2+k_y^2}$, $F_c = k_x/\sqrt{k_x^2+k_y^2}$, $Y_1 = k_{1,z}/k_0$, $Y_2 = k_{2,z}/k_0$, $Z_1 = k_{1,z}/k_0 n_1^2$, and $Z_2 = k_{2,z}/k_0 n_2^2$. t_s and t_p representing the TE wave component and TM wave component in the transmitted wave, respectively.

The transmissivity can be defined as[48]

$$T = |t_s|^2 \mathrm{Re}\left(\frac{k_{2,z}}{k_0 n_1 \cos\theta}\right) + |t_p|^2 \mathrm{Re}\left(\frac{k_{2,z}/n_2^2}{k_0 n_1 \cos\theta}\right). \quad (24)$$

3. Results and discussion

The CD is a vital parameter to measure the chiral response, which is equal to the difference in transmissivity (absorptivity/reflectivity) between LCP wave and RCP wave. We take the transmissivity into consideration in this work. Hence, the CD can be obtained from

$$\mathrm{CD} = |T_{\mathrm{LCP}} - T_{\mathrm{RCP}}|, \quad (25)$$

where T_{LCP} and T_{RCP} are the transmissivity for LCP wave and RCP wave, respectively.

Figure 2 shows the curves of transmissivity as a function of wavelength, respectively, for LCP wave, RCP wave and the corresponding CD under normal incidence. Here the relative rotation angle is fixed at 45°. The thickness values of the top and bottom slabs are both 1 μm. It can be seen that the relatively large CD appears at the wavelengths of 14.4 μm and 20.3 μm. Since the rotational symmetry and mirror symmetry have been destroyed simultaneously by the relative rotation between the two layers, the twisted bilayer α-MoO_3 is a chiral structure.

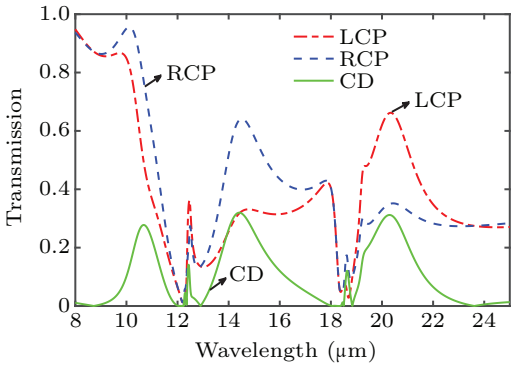


Fig. 2. Transmissivity spectrum for LCP wave (red line), RCP wave (blue line), and the corresponding CD (green line) under normal incidence, with relative rotation angle fixed at 45°.

Taking wavelength $\lambda = 14.4$ μm for example, we further enhance the CD at this wavelength. Two parameters can affect the CD, which are the thickness values of two slabs, and the relative rotation angle between them. Here, we optimize first the thickness and then the relative rotation angle. When the relative rotation angle is 45°, the transmissivity as a function of d_1 and d_2 is plotted in Fig. 3(a) for LCP wave and in Fig. 3(b) for RCP wave. Obviously, the transmissivity has the periodic enhancement with the increasing of thickness d_1 and d_2 for both LCP wave and RCP wave. The phenomenon originates from Fabry–Perót (FP) resonance. When the d_1 (or d_2) equals zero, the model is simplified into a free standing single α-MoO_3 slab. The circularly polarized wave can be decoupled into TM wave and TE wave. Besides, both of them can excite the FP resonance. The quantization condition for any two adjacent orders of FP resonances can be described as

$$\begin{aligned} \varphi + \mathrm{Re}(k_z) t_1 &= m\pi, \\ \varphi + \mathrm{Re}(k_z) t_2 &= (m+1)\pi, \end{aligned} \quad (26)$$

where φ is the reflection phase at the interface between the air and the α-MoO_3 slab, t_1 and t_2 are the thickness of the α-MoO_3 slab when the two adjacent orders of FP resonances occur, respectively, m is an integral number, $k_z = nk_0$, with n representing the refractive index and $k_0 = 2\pi/\lambda$ with wavelength λ. Therefore, the difference ($\Delta t = |t_1 - t_2|$) in thickness of the α-MoO_3 slab between the two adjacent orders of FP resonances can be calculated from

$$\Delta t = \frac{\pi}{\mathrm{Re}(k_z)}. \quad (27)$$

It is worth noting that the α-MoO_3 possesses different refractive indices in three principal directions since it is an anisotropic material. In our simulation, we define the plane of incidence as the x–z plane. Thus, the electric field vector is parallel to the y axis for the TE wave, while the x axis is for TM wave under normal incidence. According to Eq. (27), Δt is equal to 2.28 μm and 2.75 μm for TM wave and TE wave when the wavelength λ is 14.4 μm, respectively. The results are in good agreement with the scenarios in Figs. 3(a) and 3(b). Back to Fig. 3, for RCP wave, it is found that the transmissivity is enhanced periodically with the increase in d_2 when the thickness d_1 is less than 1 μm, while the transmissivity is small at the same thickness under the illumination of LCP wave. Figure 3(c) shows the corresponding CD. One can see that the CD improves periodically as d_2 increases, which comes from FP resonance as well. In addition, the CD reaches its maximum value when the thickness of top layer and bottom layer are 0.8 μm and 3.4 μm, respectively.

Based on the above optimization results ($d_1 = 0.8$ μm and $d_2 = 3.4$ μm), the influence of the relative rotation angle on circular dichroism at $\lambda = 14.4$ μm is discussed. Figure 4 shows the transmissivity under the illumination of LCP

wave, RCP wave and the corresponding CD as relative rotation angle increases from 0° to 90°. One can see that the CD is zero when the relative rotation angle equals 0°. When the relative angle becomes bigger, the CD increases gradually at first and reaches its maximum at 57°, then drops down to nearly zero when relative rotation angle approaches to 90°. Since the bilayer structure we proposed with relative rotation angle 0° or 90° possesses the rotational symmetry or mirror symmetry, the chiral response disappears. In addition, it is found that the maximum CD is smaller than 0.5. In order to acquire the stronger circular dichroism, the parameters of the model should be further optimized.

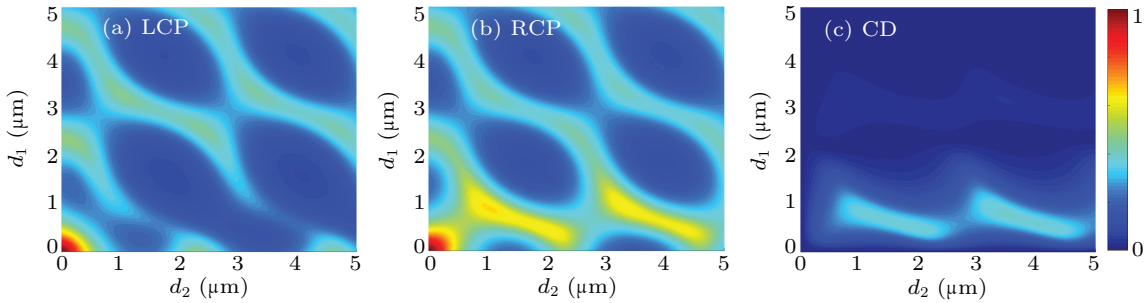


Fig. 3. Transmissivity as function of thickness of top slab d_1 and bottom slab d_2 at wavelength 14.4 μm when relative rotation angle is 45°, for (a) LCP wave, (b) RCP wave, and (c) corresponding CD.

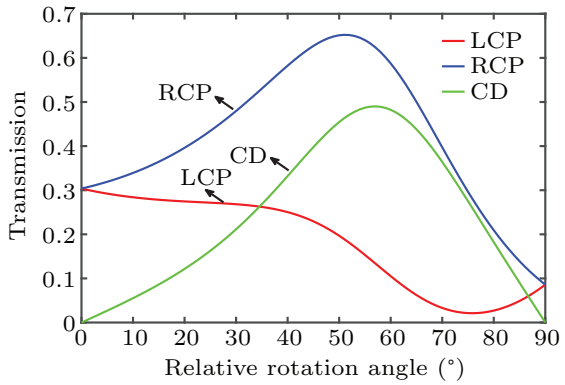


Fig. 4. Curves of transmissivity *versus* relative rotation angle for LCP wave (red line), RCP wave (blue line), and corresponding CD (green line) when thickness d_1 and d_2 are 0.8 μm and 3.4 μm, respectively.

Here, we optimize first the relative rotation angle, and then the thickness. Considering different relative rotation angles, we plot the curves of CD as a functions of thickness for the two slabs as shown in Fig. 5. It is found that the CD is extremely small at any thickness when the relative rotation angle is 10°, and the CD rises with relative rotation angle increasing. The results show that the CD can be flexibly tuned via changing the relative rotation angle between the two layers. In addition, one can see that the CD reaches its maximum value when the relative rotation angle is 70°. Therefore, we further optimize the relative rotation angle around 70° by using the same method, but the results are not shown here. It is found that the CD can reach a maximum value of 0.89 at a relative rotation angle of 75° when the thickness of the bottom slab and the top slabs are 2.72 μm and 0.6 μm, respectively.

Now, at the optimized parameters ($\phi = 75°$, $d_1 = 0.6$ μm and $d_2 = 2.72$ μm), the transmissivity spectra and CD spectra are investigated and shown in Fig. 6. At a wavelength of 14.4 μm, a large transmissivity can be observed for RCP wave while the transmissivity is almost zero for LCP wave. One can see that the CD can reach 0.89, indicating a strong chirality.

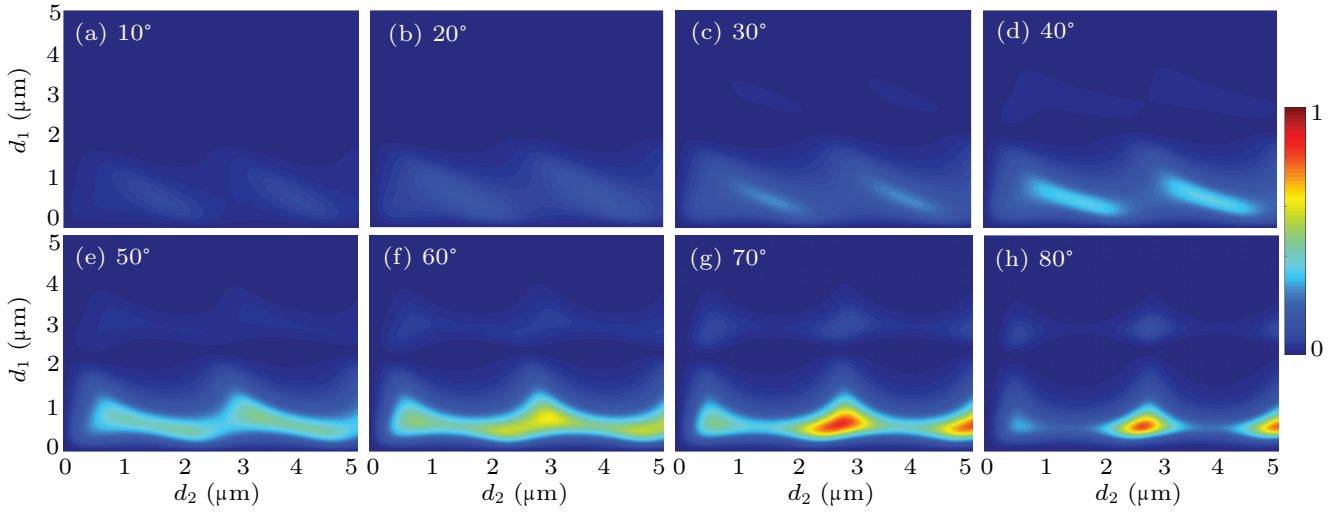


Fig. 5. Variations of CD with thickness of top slab d_1 and bottom slab d_2 at different relative rotation angles: (a) 10°, (b) 20°, (c) 30°, (d) 40°, (e) 50°, (f) 60°, (g) 70°, and (h) 80°.

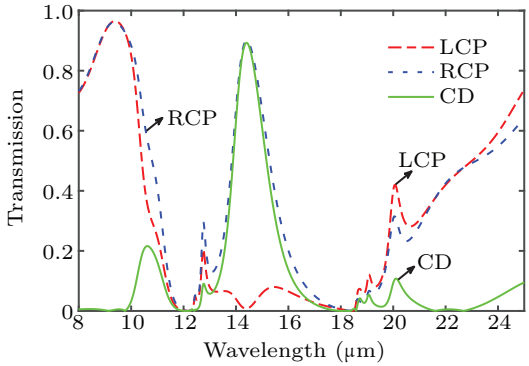


Fig. 6. Transmissivity spectrum for LCP wave (red line), RCP wave (blue line), and the corresponding CD (green line), with relative rotation angle being 75°, and top slab and bottom slab 0.6 μm and 2.72 μm in thickness, respectively.

To better illustrate the underlying physical mechanisms of the strong chirality, the polarization conversion curves for LCP wave and RCP wave under normal incidence are shown in Fig. 7. When circularly polarized light with different handedness is incident on the structure, the transmitted wave contains the components of both LCP wave and RCP wave. For the incident RCP wave, the amplitude of LCP wave in the transmitted wave is greater than 0.4 at a wavelength of 14.4 μm, and the amplitude of RCP wave reaches 0.5. However, both LCP wave and RCP wave in transmitted wave are close to zero under the illumination of LCP wave. It can be found that there is a huge difference in polarization conversion efficiency between the two circularly polarized waves, resulting in the strong circular dichroism in Fig. 6. Nevertheless, we can also find that no matter whether it is incident LCP wave or RCP wave, the difference between polarization conversion and no polarization conversion in the transmitted wave is very small. Hence, their physical mechanisms can be further studied.

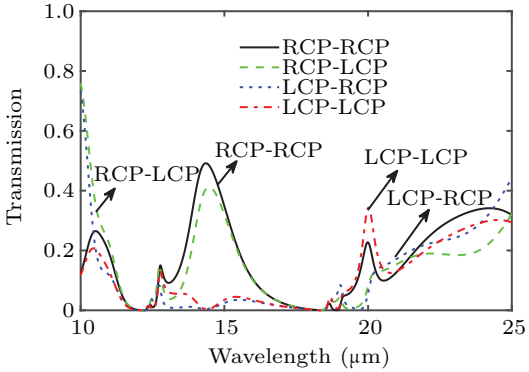


Fig. 7. Components of LCP wave and RCP wave in transmitted wave.

To further explain the strong chirality of the bilayer structure, the components of TE wave and TM wave of the transmitted wave for normal incidence of an LCP wave and an RCP wave are shown in Figs. 8(a) and 8(b). Here, the wavelength we concerned is still 14.4 μm. It is found that the TM component in the transmitted wave is relatively small for an incident LCP wave, while the TM component can reach 0.9 for an incident RCP wave at the wavelength of 14.4 μm. Moreover, one can see that the TE component in the transmitted wave is almost zero for both the incident LCP wave and the incident RCP wave in a wavelength range from 11.8 μm to 18.3 μm. According to Ref. [49], the response of the structure for normal incidence of the TE wave and the TM wave are related to ε_y and ε_x, respectively. Since the sign of the real part of the ε_y is negative in the wavelength range of 11.8 μm–18.3 μm, now the α-MoO_3 behaves like metal, resulting in a strong reflection for TE wave. Thus, the anisotropic properties of the α-MoO_3 guarantee the giant chirality of the bilayer structure.

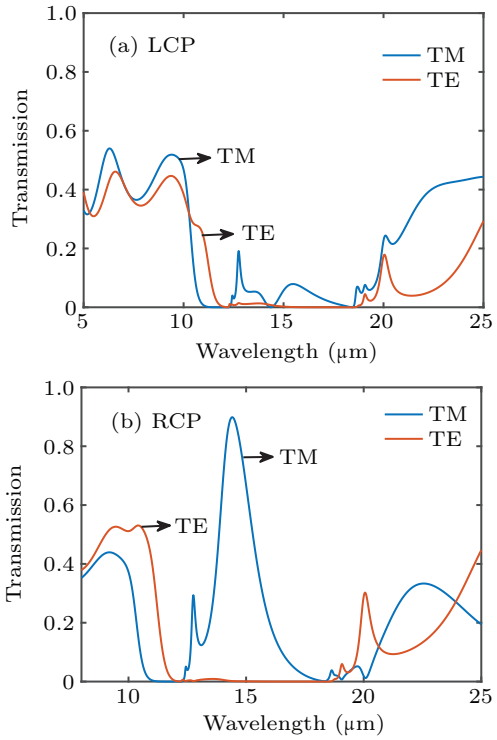


Fig. 8. Components of TE wave and TM wave in transmitted waves: (a) LCP wave and (b) RCP wave.

Here, the influence of the relative rotation angle on CD is discussed in the same situation as that in Fig. 6, and displayed in Fig. 9. As the relative rotation angle increases, the CD slowly rises from 0 to the maximum value 0.89, and then decreases to nearly zero when the relative rotation angle is close to 90°. It is worth noting that the structure can still maintain strong CD over 0.8 when the relative rotation angle approximately ranges from 69° to 80°. Therefore, the CD is not very sensitive to the relative rotation angle, which reduces the requirement for angle in fabrication.

In fact, the influence of incident angle on the chirality is of vital importance. Thus, it is necessary to keep strong circular dichroism even at a large incident angle. Based on the optimized results as shown in Fig. 10, we discuss the transmissivity and CD varying with incident angle. When the in-

cident angle increases from 0° to 90°, the transmissivity for LCP wave always keeps a low level while the transmissivity for RCP wave first maintains a large value and then decreases. It can be seen from the green line in Fig. 10 that the CD can be larger than 0.85 when the incident angle is smaller than 40°, indicating that the chirality of the structure is robust against the incident angle.

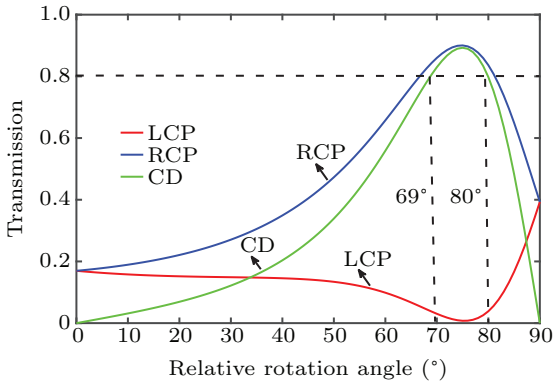


Fig. 9. Curves of transmissivity *versus* relative rotation angle for LCP wave for LCP wave (red line), RCP wave (blue line), and the corresponding CD (green line), with bottom slab and top slab being 0.6 μm and 2.72 μm in thickness, respectively.

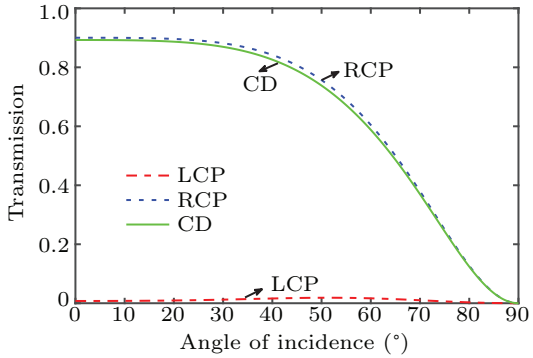


Fig. 10. Curve of transmissivity *versus* incident angle for LCP wave (red line), RCP wave (blue line), and the corresponding CD (green line), with wavelength being 14.4 μm, and bottom slab and top slabs 0.6 μm and 2.72 μm in thickness, respectively.

4. Conclusions

In summary, a chiral structure based on twisted bilayer α-MoO_3 has been proposed and investigated. Through the optimization of parameters, the circular dichroism of the structure can reach 0.89. To reveal more in-depth physical mechanism, we analyze the polarization conversion between LCP wave and RCP wave. Furthermore, we discuss the influence of the relative rotation angle and the angle of incidence on the CD. The results show that the CD can keep a high level (CD$>$ 0.8) when the relative rotation angle approximately ranges from 69° to 80°. Besides, the CD is robust against the incident angle. It is believed that this work not only provides a new idea for chiral structure, but also promotes the development of the manipulation of circularly polarized wave.

Acknowledgements

Project supported by the Training Program of the Major Research Plan of the National Natural Science Foundation of China (Grant No. 92052106), the National Natural Science Foundation of China (Grant Nos. 61771385 and 52106099), the Science Foundation for Distinguished Young Scholars of Shaanxi Province, China (Grant No. 2020JC-42), the Science and Technology on Solid-State Laser Laboratory, China (Grant No. 6142404190301), the Science and Technology Research Plan of Xi'an City, China (Grant No. GXYD14.26), the Shandong Provincial Natural Science Foundation, China (Grant No. ZR2020LLZ004), and the Start-Up Funding of Guangdong Polytechnic Normal University, China (Gtrant No. 2021SDKYA033).

References

[1] Sharma V, Crne M, Park J O and Srinivasarao M 2009 *Science* **325** 449
[2] Martens K, Binkowski F, Nguyen L, Hu L, Govorov A O, Burger S and Liedl T 2021 *Nat. Commun.* **12** 2025
[3] Kleinlogel S and White A G 2008 *PLoS One* **3** e2190
[4] Liu T, Besteiro L V, Liedl T, Correa-Duarte M A, Wang Z and Govorov A O 2019 *Nano Lett.* **19** 1395
[5] Yu P, Wang B, Wu X, Wang W, Xu H and Wang Z 2020 *Acta Phys. Sin.* **69** 207101 (in Chinese)
[6] Hendry E, Carpy T, Johnston J, Popland M, Mikhaylovskiy R V, Lapthorn A J, Kelly S M, Barron L D, Gadegaard N and Kadodwala M 2010 *Nat. Nanotechnol.* **5** 783
[7] Singh A, Kaur N and Chopra H K 2019 *Crit. Rev. Anal. Chem.* **49** 553
[8] Kwon D, Werner P L and Werner D H 2008 *Opt. Express* **16** 11802
[9] Tang Y and Cohen A E 2010 *Phys. Rev. Lett.* **104** 163901
[10] Wu X, Fu C and Zhang Z M 2020 *ES Energy Environ.* **8** 5
[11] Yoo S and Park Q 2015 *Phys. Rev. Lett.* **114** 203003
[12] Upadhyay S S, Gadhari N S and Srivastava A K 2020 *Biosens. Bioelectron.* **165** 112397
[13] Wu Z, Chen X, Wang M, Dong J and Zheng Y 2018 *ACS Nano* **12** 5030
[14] Ma W, Kuang H, Xu L, Ding L, Xu C, Wang L and Kotov N A 2013 *Nat. Commun.* **4** 2689
[15] Hu L, Cheng F, Tang Y and Wang H 2021 *Eur. Phys. J. B* **94** 8
[16] Chen Y, Gao J and Yang X 2018 *Nano Lett.* **18** 520
[17] Li Z and Wang Z F 2020 *Chin. Phys. B* **29** 107101
[18] Xiao W, Shi X, Zhang Y and Zeng Y 2019 *Phys. Scr.* **94** 085501
[19] He T, Ye Q and Song G 2020 *Chin. Phys. B* **29** 097306
[20] Kong X, Khorashad L K, Wang Z and Govorov A O 2018 *Nano Lett.* **18** 2001
[21] Liu C, Wu F, Jiang Q, Chen Y and Yin C 2020 *Eur. Phys. J. B* **93** 197
[22] Wang Z, Jia H, Yao K, Cai W, Chen H and Liu Y 2016 *ACS Photon.* **3** 2096
[23] Svirko Y, Zheludev N and Osipov M 2001 *Appl. Phys. Lett.* **78** 498
[24] Rogacheva A V, Fedotov V A, Schwanecke A S and Zheludev N I 2006 *Phys. Rev. Lett.* **97** 177401
[25] Plum E, Fedotov V A, Schwanecke A S, Zheludev N I and Chen Y 2007 *Appl. Phys. Lett.* **90** 223113
[26] Decker M, Klein M W, Wegener M and Linden S 2007 *Opt. Lett.* **32** 856
[27] Wu X, Fu C and Zhang Z M 2019 *Opt. Commun.* **452** 124
[28] Gao W, Leung H M, Chen H and Tam W Y 2011 *J. Opt.* **13** 115101
[29] Bai Y, Wang Y, Chen Y, Zhang Y, Fu T, Zhang Z and Wan L 2018 *Optik* **154** 165
[30] He G, Shang X, Yue J, Zhai X, Xia S, Li H and Wang L 2020 *J. Opt. Soc. Am. B* **37** 927
[31] Ullah H, Abudukelimu A, Qu Y, Bai Y, Aba T and Zhang Z 2020 *Nanotechnology* **31** 275205
[32] Shi J, Liu X, Yu S, Lv T, Zhu Z, Ma H F and Cui T J 2013 *Appl. Phys. Lett.* **102** 191905

[33] Lv T, Chen X, Dong G, Liu M, Liu D, Ouyang C, Zhu Z, Li Y, Guan C, Han J, Zhang W, Zhang S and Shi J 2020 *Nanophotonics* **9** 3235
[34] Dong J, Zhou J, Koschny T and Soukoulis C 2009 *Opt. Express* **17** 14172
[35] Poddubny A, Iorsh I, Belov P and Kivshar Y 2013 *Nat. Photon.* **7** 948
[36] Shekhar P, Atkinson J and Jacob Z 2014 *Nano Converg.* **1** 14
[37] Takayama O and Lavrinenko A V 2019 *J. Opt. Soc. Am. B* **36** F38
[38] Chen M, Lin X, Dinh T H, Zheng Z, Shen J, Ma Q, Chen H, Jarillo-Hereero P and Dai S 2020 *Nat. Mater.* **19** 1307
[39] Wu B, Wang M, Wu F and Wu X 2020 *Appl. Opt.* **60** 4599
[40] Zhou C, Wu X, Zhang Y, Yi H and Antezza M 2021 *Phys. Rev. B* **103** 155404
[41] Zhou C, Wu X, Zhang Y, Xie M and Yi H 2021 *Appl. Phys. Lett.* **118** 173103
[42] Zhou C, Yang S, Zhang Y and Yi H 2020 *Nanoscale Microscale Thermophys. Eng.* **24** 168
[43] Wei C and Cao T 2021 *J. Phys. D* **54** 234005
[44] Lin X, Liu Z, Stauber T, Gómez-Santos G, Gao F and Chen H 2020 *Phys. Rev. Lett.* **125** 077401
[45] Stauber T, Low T and Gómez-Santos G 2018 *Phys. Rev. Lett.* **120** 046801
[46] Wu X, Fu C and Zhang Z M 2020 *J. Heat Transfer* **142** 072802
[47] Wu X and Fu C 2018 *Nanoscale Microscale Thermophys. Eng.* **22** 114
[48] Moharam M G, Grann E B and Pommet D A 1995 *J. Opt. Soc. Am.* **12** 1068
[49] Wu X, Jin C and Fu C 2017 *Opt. Commun.* **402** 507